Chromophore Structure of Cyanobacterial Phytochrome Cph1 in the Pr State: Reconciling Structural and Spectroscopic Data by QM/MM Calculations

Maria Andrea Mroginski,[†*] David von Stetten,[†] Francisco Velazquez Escobar,[†] Holger M. Strauss,[‡] Steve Kaminski,[†] Patrick Scheerer,[§] Mina Günther,[†] Daniel H. Murgida,[¶] Peter Schmieder,[‡] Christian Bongards,[‖] Wolfgang Gärtner,[‖] Jo Mailliet,[*] Jon Hughes,[*] Lars-Oliver Essen,[††] and Peter Hildebrandt[†*]

[†]Technische Universität Berlin, Institut für Chemie, [‡]Leibniz-Institut für Molekulare Pharmakologie, and [§]Institut für Medizinische Physik und Biophysik, Charité-Universitätsmedizin Berlin, Berlin, Germany; [¶]INQUIMAE, Departamento de Química Inorgánica, Analítica y Química Física, Facultad de Ciencias Exactas y Naturales, Universidad de Buenos Aires, Buenos Aires, Argentina; [‖]Max-Planck-Institut für Bioanorganische Chemie, Mülheim, Germany; [**]Plant Physiology, Justus-Liebig University Gießen, Giessen, Germany; and [††]Structural Biochemistry, Department of Chemistry, Philipps University Marburg, Marburg, Germany

ABSTRACT A quantum mechanics (QM)/molecular mechanics (MM) hybrid method was applied to the Pr state of the cyanobacterial phytochrome Cph1 to calculate the Raman spectra of the bound PCB cofactor. Two QM/MM models were derived from the atomic coordinates of the crystal structure. The models differed in the protonation site of His^{260} in the chromophore-binding pocket such that either the δ-nitrogen (M-HSD) or the ε-nitrogen (M-HSE) carried a hydrogen. The optimized structures of the two models display small differences specifically in the orientation of His^{260} with respect to the PCB cofactor and the hydrogen bond network at the cofactor-binding site. For both models, the calculated Raman spectra of the cofactor reveal a good overall agreement with the experimental resonance Raman (RR) spectra obtained from Cph1 in the crystalline state and in solution, including Cph1 adducts with isotopically labeled PCB. However, a distinctly better reproduction of important details in the experimental spectra is provided by the M-HSD model, which therefore may represent an improved structure of the cofactor site. Thus, QM/MM calculations of chromoproteins may allow for refining crystal structure models in the chromophore-binding pocket guided by the comparison with experimental RR spectra. Analysis of the calculated and experimental spectra also allowed us to identify and assign the modes that sensitively respond to chromophore-protein interactions. The most pronounced effect was noted for the stretching mode of the methine bridge A-B adjacent to the covalent attachment site of PCB. Due a distinct narrowing of the A-B methine bridge bond angle, this mode undergoes a large frequency upshift as compared with the spectrum obtained by QM calculations for the chromophore in vacuo. This protein-induced distortion of the PCB geometry is the main origin of a previous erroneous interpretation of the RR spectra based on QM calculations of the isolated cofactor.

INTRODUCTION

Sensory photoreceptors utilize light as a source of information to regulate physiological processes (1). Phytochromes, a family of red-light-sensitive photoreceptors, carry an open-chain tetrapyrrole chromophore attached to the protein via a thioether bond to a Cys residue (Fig. 1). Originally, phytochromes were thought to be restricted to higher plants, but then representatives of this family were also discovered in various prokaryote lineages and in fungi (2,3). Prokaryotic and fungal phytochromes share many similarities with plant phytochromes, including the overall mechanism of the photoinduced reaction cycle that reversibly transforms the receptor from one stable state (Pr) to another (Pfr), thereby constituting a switch between a physiologically inactive and an active form. The first step of the reaction cycle involves a photoisomerization of a methine bridge double bond of the tetrapyrrole (1,4). Subsequent relaxation processes, including a transient deprotonation of the chromophore, eventually lead to major changes of the protein structure that complete the conversion.

Until recently, structural information about phytochromes and specifically about the active center was obtained predominantly by spectroscopic methods. Among these, resonance Raman (RR) spectroscopy has turned out to be a particularly powerful technique because it selectively probes the vibrational bands of the chromophore upon (pre-)resonant excitation (5–25). In this way, a lot of valuable structural data about the chromophore and its interactions with the protein environment were obtained for the various (intermediate) states of the phytochrome photocycle. Special attention has been paid to the structure of the chromophore in the parent states Pr and Pfr. On the basis of QM calculations, the RR spectrum of

Submitted December 3, 2008, and accepted for publication February 5, 2009.

*Correspondence: andrea.mroginski@tu-berlin.de or hildebrandt@chem.tu-berlin.de

Holger M. Strauss's present address is Nanolytics GmbH, Potsdam, Germany.

Abbreviations: Agp1, phytochrome from *Agrobacterium tumefaciens*; *α-CPC*, *α-subunit of C-phycocyanin*; BV, biliverdin IX*α*; B3LYP, three-parameter exchange functional according to Becke, Lee, Yang, and Parr; DFT, density functional theory; DrBphP, phytochrome from *Deinococcus radiodurans*; GAF, domain found in cGMP-specific phosphodiesterases; MM, molecular mechanics; MD, molecular dynamics; N-H ip, N-H in-plane bending; PCB, phycocyanobilin; PED, potential energy distribution; phyA, plant phytochrome; Pr, Pfr, red- and far-red absorbing parent states of phytochrome; P*ΦB*, phytochromobilin; QM, quantum mechanics; RMSD, root mean-square deviation; RR, resonance Raman.

Editor: Janos K. Lanyi.

0006-3495/09/05/4153/11 $2.00

doi: 10.1016/j.bpj.2009.02.029

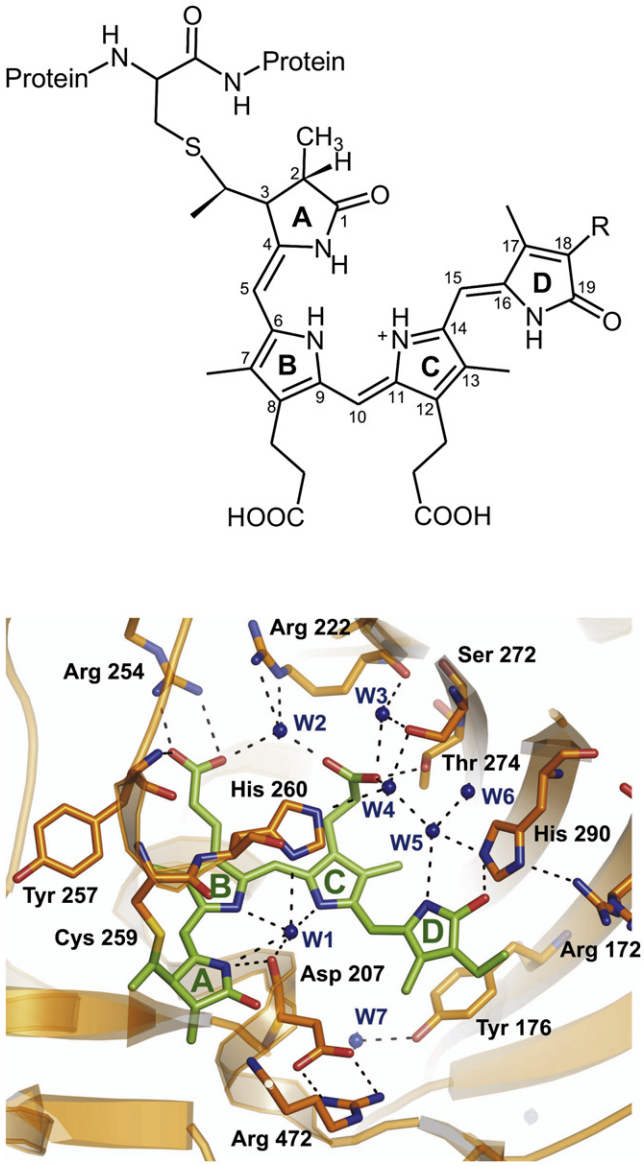

FIGURE 1 Structural formula of the PCB chromophore ($R = C_2H_5$) including the ring and atom labeling (*top*) and a presentation of the chromophore-binding pocket according to the crystal structure (29) (*bottom*).

the Pr state of plant phytochrome phyA was interpreted in terms of ZZZasa geometry (14–16,18,20), an assignment that was further supported by the pattern of isotopic shifts brought about by site-directed ^{2}H- and ^{13}C-labeling of the chromophore by chemical synthesis (21).

The first x-ray structures of the Pr states of the bacterial phytochromes DrBphP (*Deinococcus radiodurans*) and RpBphP3 (*Rhodopseudomonas palustris*) (26–28), however, revealed a different picture inasmuch as the methine bridge A-B adjacent to the thioether linkage of ring A was shown to be in a *syn* conformation, in contrast to the *anti* conformation suggested by the RR spectra and QM calculations (18,20,21). To account for this discrepancy, it has been suggested that the cofactor geometries of the BV-binding bacteriophytochromes, such as DrBphP and RpBphP3, differ from those of PΦB-binding plant phytochrome phyA (21). Specifically, the different covalent attachment sites for BV and PΦB at either an N-terminal cysteine (Cys^{24}) or a cysteine within the chromophore-binding GAF domain (Cys^{321}) have been proposed to stabilize a ZZZssa structure in bacterial phytochromes and a ZZZasa structure in plant phytochromes, respectively.

With the recent elucidation of the three-dimensional structure of the Pr state of the cyanobacterial phytochrome Cph1, which also unambiguously shows a ZZZssa chromophore geometry (Fig. 1) (29), this interpretation appears to be superseded. Cph1 is more closely related to phyA and other plant phytochromes than are bacterial phytochromes, in particular because it uses the same Cys for covalent binding of the chromophore (PΦB in plants, PCB in Cph1). Moreover, the experimental RR spectra of Cph1 and phyA are very similar (13).

An alternative explanation may be based on possible differences between the cofactor geometries in phytochromes in the crystalline state and in solution to which the spectroscopic techniques usually refer. However, a comparative RR spectroscopic study performed with DrBphP and Agp1 from *Agrobacterium tumefaciens* ruled out structural differences on the level of methine bridge conformations (24). Furthermore, recent NMR spectroscopic studies on Cph1 are consistent with the ZZZssa geometry in the Pr state (30,31).

In view of these results, a critical reconsideration of the analysis and interpretation of the RR data is clearly necessary. In previous studies, we calculated the Raman spectra of isolated tetrapyrroles in a large number of different conformations and configurations on the basis of density functional theory (DFT) employing scaled force fields (18,20,21). A comparison of the various calculated spectra with the experimental RR spectra of the Pr state obtained from phyA adducts with PΦB, PCB, and PCB isotopomers revealed the best agreement for the ZZZasa geometry (20,24). Calculated vibrational spectra obtained by this approach reproduce the experimental spectra of organic molecules, including tetrapyrroles, with remarkable accuracy (21,32–34). However, such QM calculations cannot take into account the protein environment for tetrapyrroles as bound in phytochromes. Thus, the inevitable neglect of possible perturbations on the electronic and structural properties of the chromophore is certainly the most severe approximation of the QM-based interpretation of the RR spectra of phytochromes.

With the availability of the three-dimensional structures of the Pr state of phytochromes, hybrid methods can now be employed (35), and were recently adapted to cofactor-protein complexes including a tetrapyrrole-binding protein, α-C-phycocyanin (36). These calculations reproduced the experimental RR spectra in an excellent manner. Hybrid methods combine QM calculations of the cofactor with MM calculations of the remainder of the protein and the solvent shell. In this way, protein-cofactor interactions are explicitly considered.

We present here the application of the QM/MM methodology to the Pr state of Cph1. The central goal is to analyze the relationship among protein-cofactor interactions, chromophore structure, and RR spectra. The experimental part of this study includes 1), a comparative analysis of the RR spectra of crystals and solutions of the Cph1 sensory module (Cph1Δ2) to determine possible differences in their cofactor structures; and 2), the determination of isotopic effects in RR spectra of Cph1Δ2 adducts with ^{13}C-labeled PCB to identify the modes indicative of conformation at the A-B methine bridge. The theoretical part of the study is based on two QM/MM models that are derived from the crystallographic data and differ primarily in the orientation of His^{260} in close vicinity of the chromophore. The Raman spectra calculated from these models are compared with the experimental spectra and the QM-calculated spectra of the isolated chromophores. This analysis allows for the identification of those structural parameters that are affected by the interactions with the surrounding protein matrix and cause critical changes in the Raman spectra. Finally, we discuss the potential of this combined QM/MM and RR spectroscopic approach for refining the current crystallographic structural model at the cofactor site.

MATERIALS AND METHODS

Protein expression and crystallization

Cph1Δ2, the his-tagged sensory module (residues 1–514) of Cph1 phytochrome from the cyanobacterium *Synechocystis* 6803, was overexpressed in *Escherichia coli* either as holoprotein (37) or apoprotein for subsequent in vitro autoassembly with the chromophore. Cph1Δ2 holoprotein crystals were generated as previously described (29).

Isotope labeling of PCB and holoprotein reconstitution

The synthesis of ^{13}C(5)-labeled PCB has been described elsewhere (38). Unlabeled PCB was obtained by methanolysis of freeze-dried *Spirulina* in analogy to the procedure described by Strauss et al. (39) and purified by preparative reverse-phase high-performance liquid chromatography. [^{15}N]PCB was produced and assembled with apo-Cph1Δ2 as previously described (39). ^{13}C(5)-labeled PCB was assembled in a 5:1 molar ratio with recombinant his-tagged Cph1Δ2.

RR spectroscopy

RR spectra of the Pr state of Cph1Δ2 solutions and crystals were obtained with 1064-nm excitation at -140°C as described in detail elsewhere (19,22,24) (see Supporting Material).

Theoretical calculations

Calculation of the vibrational spectra of protein cofactors at a QM/MM level of theory requires three basic steps (36). The first step consists of MD simulations of the entire protein in a water box to search for a low-energy conformation of the solvated system. These simulations are carried out with fixed cofactor (chromophore) geometry. The geometry of the cofactor and its immediate environment is optimized in a second step at a higher level of theory at which the cofactor is described with DFT, and the environment is described with a MM force field. Finally, in a third step, the spectroscopic properties of the cofactor embedded in the protein matrix are computed using a QM (i.e., DFT) approach. These three steps are described in detail in Figs. S1–S4 of the Supporting Material.

RESULTS AND DISCUSSION

QM/MM-optimized structures

The structure of the protein dissolved in water was obtained by QM/MM optimization after a 6-ns MD simulation. No (partial) collapse of the protein structure was noted, and the system was thermally equilibrated as judged on the basis of the temporal evolution of various energy terms (Fig. S6). Specifically, the structures of the water network did not fluctuate any more after 1.5 ns. Furthermore, in general, there were only small differences with respect to the crystal structure (Figs. S5, S7, S8). The only exceptions refer to the loop regions such that the total RMSD of the M-HSD and M-HSE model is 2.49 Å. In the chromophore-binding pocket, the deviations are much smaller (Fig. 2) and the RMSD for the PCB chromophore is only 0.35 Å and 0.28 Å for the M-HSD and M-HSE model, respectively. These are models based on different protonation patterns of His^{260}, with the δ- and ε-nitrogen carrying a proton in M-HSD and M-HSE, respectively.

The change of the protonation site of His^{260} has a significant effect on the orientation of its imidazole ring with respect to rings B and C of the PCB cofactor (Fig. 3; for the PCB nomenclature, see Fig. 1). In the M-HSD model, His^{260} adopts a nearly parallel orientation with a deviation from coplanarity of $-7°$ compared with $+7°$ in the crystal structure model. In the M-HSE model, His^{260} is tilted with respect to the PCB plane (i.e., rings B and C) by ~50°. This rotation of His^{260} does not induce major structural changes in the chromophore compared with both the M-HSD and the crystal structure model (vide infra), but it disturbs the water network in the cavity formed by the four pyrrolic rings. In the M-HSE model, the central water molecule (pyrrole water) interacts with the N-H group of ring A, and with Nδ of His^{260}, whereas the N-H groups of rings B and C form hydrogen bonds with the

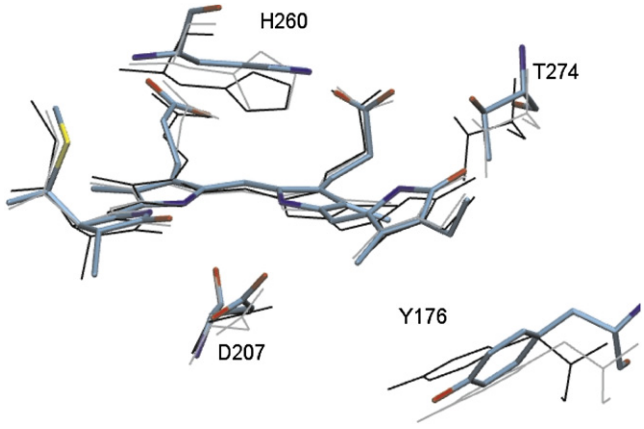

FIGURE 2 Comparison of the structures of the chromophore-binding site obtained from the crystal structure (29) (*black*) and optimized by QM/MM calculations for the M-HSE (*gray*) and M-HSD (*light-blue*) models.

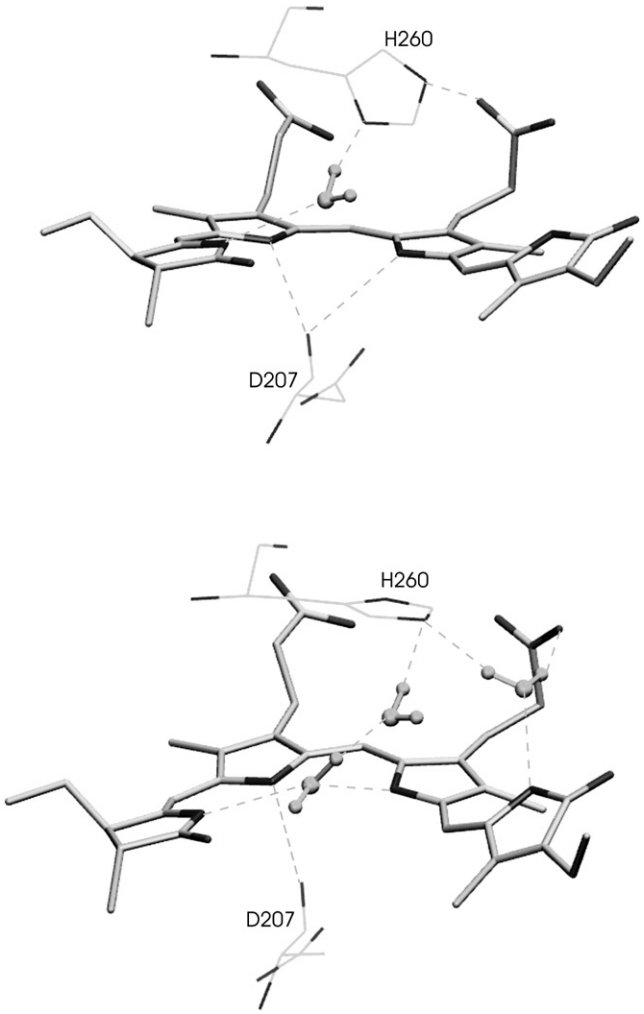

FIGURE 3 Water network inside the tetrapyrrole cavity in the M-HSE (*top*) and M-HSD (*bottom*) models.

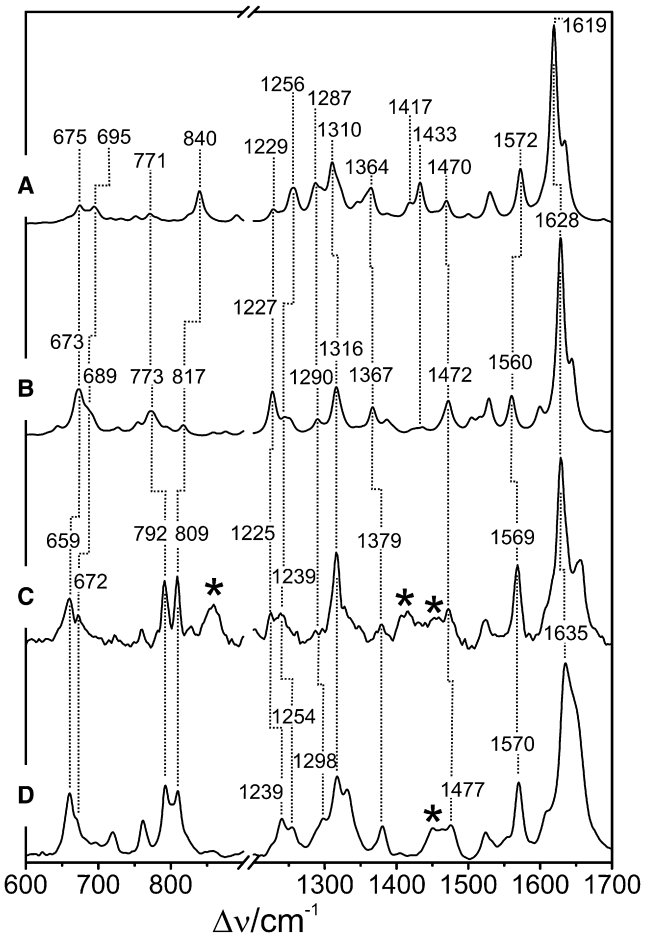

FIGURE 4 Experimental RR spectra of the Pr state of Cph1Δ2 compared with Raman spectra obtained from QM/MM calculations in the frequency range of 600–1700 cm^{-1}. (*A*) Calculated Raman spectrum of the M-HSE model. (*B*) Calculated Raman spectrum of the M-HSD model. (*C*) Experimental RR of Cph1Δ2 crystals. (*D*) Experimental RR spectrum of frozen Cph1Δ2 solution. The experimental spectra were obtained with 1064-nm excitation at −140°C. Asterisks denote residual buffer and protein bands.

backbone C = O function of Asp^{207}. In the M-HSD model, His^{260} interacts with the chromophore through at least three water molecules. The pyrrole water forms hydrogen bonds with rings A and C and is linked to His^{260} via an additional water molecule. The N-H group ring B interacts directly with the C=O group of Asp^{207}. Furthermore, His^{260} indirectly interacts through a water bridge with ring D, whereas no direct or indirect ring D to His^{260} interactions are predicted within the M-HSE model. The latter displays a well-defined hydrogen bond between Nε of His^{260} and the COO^- group of the propionic side chain of ring C. In the M-HSD model, this hydrogen bond is replaced by a water bridge (see Fig. S8 and Table S1 for further details).

RR spectra of Cph1Δ2 crystals and solutions

RR spectra of the Pr state of Cph1Δ2 were obtained at −140°C from both crystalline and frozen solution samples (Fig. 4). The spectrum of crystalline Cph1Δ2 was measured from several microcrystals (~10–20 μm), grown under conditions as used for x-ray diffraction experiments. The raw spectra included large spectral contributions from the cryogenic buffer that could not be completely subtracted. However, the residual bands of the buffer and the Raman bands of the protein matrix (all marked by asterisks) do not obscure the chromophore RR bands that are particularly indicative of the tetrapyrrole configuration and conformation. These are specifically the bands in the region between 1500 and 1700 cm^{-1} that are spectral markers for the methine bridge geometry and the protonation state of the tetrapyrrole (marker band region (18,20), vide infra), and in the regions between 600 and 900 cm^{-1} and between 1200 and 1400 cm^{-1} that reflect more subtle structural details of the chromophore and its interactions with the protein environment.

The experimental RR spectra of Cph1Δ2 crystals and frozen solution are very similar, although some small differences are detectable that cannot be exclusively attributed to

the expected band narrowing in the crystal spectrum. Most notable are the frequency shifts in the marker band region (Fig. 5). In the crystal spectrum, the strongest band is observed at 1628 cm^{-1} and thus at a frequency lower by 7 cm^{-1} than in the solution spectrum, whereas its high-frequency shoulder is upshifted by 7 cm^{-1}. As a result of these shifts and the band narrowing, both bands are more clearly separated in the crystal as compared with the solution spectrum. The origin of these remarkable shifts is not clear, but differences in the methine bridge geometry can be ruled out in view of the very good agreement in other regions of the spectrum. Also, the protonation state is the same, as indicated by the band at 1569 (1570) cm^{-1}, which is a marker for the protonated (cationic) tetrapyrrole. Minor spectral alterations refer, for instance, to the weak bands at 1225 and 1239 cm^{-1} in the crystal spectrum (Fig. 4), which shift to higher frequencies in solution, and the band at 1298 cm^{-1} in the solution spectrum, which can hardly be detected in the crystal spectrum.

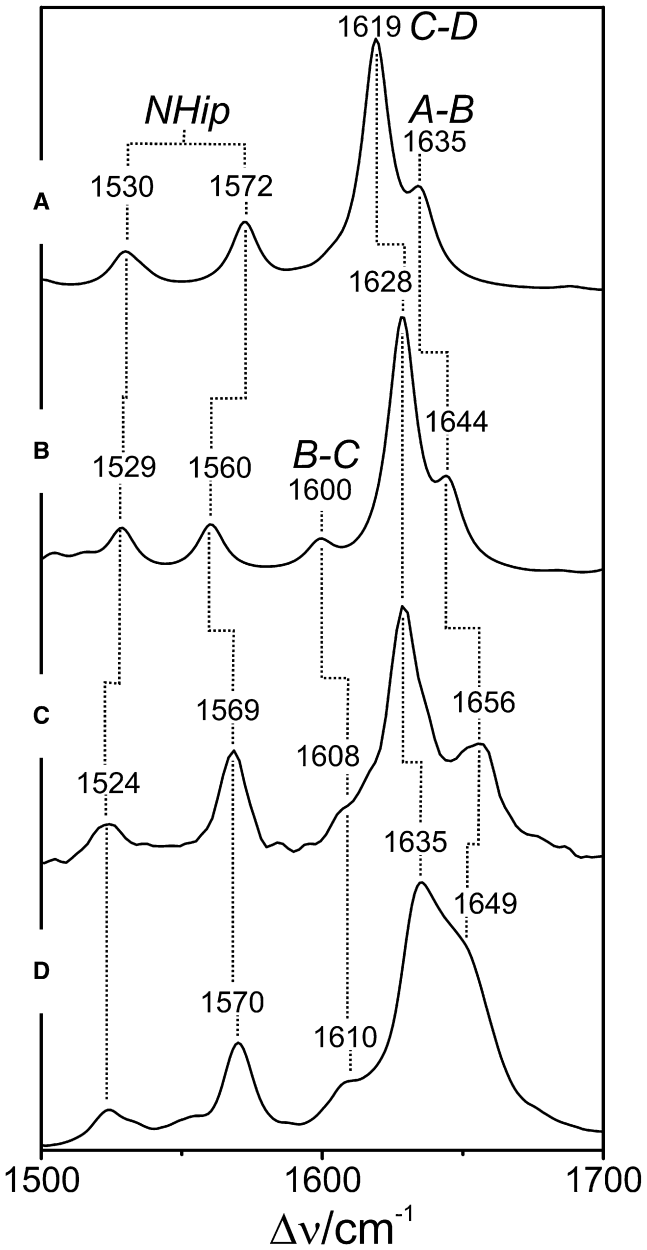

FIGURE 5 Experimental RR spectra of the Pr state of Cph1Δ2 compared with Raman spectra obtained from QM/MM calculations in the region of the marker bands. (*A*) Calculated Raman spectrum of the M-HSE model. (*B*) Calculated Raman spectrum of the M-HSD model. (*C*) Experimental RR of Cph1Δ2 crystals. (*D*) Experimental RR spectrum of a frozen Cph1Δ2 solution. The experimental spectra were obtained with 1064-nm excitation at −140°C.

QM/MM calculations

The calculated Raman spectra obtained for both M-HSE and M-HSD models provide a good description of the overall vibrational band pattern of the experimental RR spectra (Fig. 4). However, the calculated Raman spectra notably differ in some details. In the marker band region, the most intense experimental RR bands at 1628 (1635) and 1656 (1649) cm^{-1} of Cph1Δ2 crystals (solution) are much better reproduced by the M-HSD model spectrum (Fig. 5). Here, two closely spaced modes at 1629 and 1626 cm^{-1}, which include the C=C stretching coordinates of the C-D methine bridge and ring D, give rise to a strong band at 1628 cm^{-1}, whereas a second medium-intense band at 1645 cm^{-1} originates from the C=C stretching of the A-B methine bridge (Table 1). For the M-HSE model, two related modes are predicted at distinctly lower frequencies, whereas the relative intensities of the experimental bands are equally well reproduced by the spectra of both models.

Further differences between the calculated spectra refer, for instance, to the modes involving inter alia the N-H out-of-plane deformation of rings B and C, which give rise to a doublet at 675 and 695 cm^{-1} in the M-HSE spectrum (Fig. 4). The frequencies and intensities of these modes are altered in the M-HSD model (673 and 689 cm^{-1}), which reproduces the experimental band pair at 659 and 672 cm^{-1} quite well. The C-H out-of-plane mode of the C-D methine bridge is calculated to be at 840 cm^{-1} in the M-HSE model, but its frequency is predicted to be lower by 23 cm^{-1} in the M-HSD model such that the latter agrees well with the experimental band at 809 cm^{-1}. The adjacent RR band at 792 cm^{-1} is then attributed to C-H out-of-plane of the B-C methine bridge deformation, which for both models is calculated too low in frequency. For both deformation modes, the intensities are underestimated.

Particularly remarkable are the differences in the region between 1200 and 1350 cm^{-1}, which refer to modes contributing to bands at 1229, 1287, 1256, 1310, 1417, and 1433 cm^{-1} for the M-HSE model. In the M-HSD model the counterparts are, in part, composed rather differently, leading to different predicted intensities and frequencies. Many of these modes include the C-N stretching and N-H in-plane bending coordinates of the four pyrrole rings. Again, also in this region the spectrum calculated for the M-HSD model provides a better description of the

TABLE 1 Calculated vibrational modes of the protein-bound PCB in the M-HSD and M-HSE models, and the isolated PCB in the ZZZssa configuration

QM/MM calculations				QM calculations	
M-HSD		M-HSE		ZZZssa*	
ν (I)	PED	ν (I)	PED	ν (I)	PED
1645 (32)	46 AB str 13 BC str 7 ring A str 5 N-H ip A 6 C-H ip AB	1635 (31)	48 AB str 5 BC str 7 ring A str 10 N-H ip A 7 C-H ip AB	1636 (100)	63 CD str 7 ring D str 10 C-H ip CD
1629 (100)	26 ring D str 38 CD str 6 ring D bend 6 N-H ip D	1619 (100)	8 ring D str 56 CD str 11 C-H ip CD	1627 (18)	67 D str
1626 (15)	54 ring D str 19 CD str	1603 (4)	81 ring D str	1622 (39)	35 BC str 18 AB str 12 C-H ip BC
1599 (12)	41 BC str 10 AB str 13 C-H BC ip	1592 (2)	36 BC str 5 AB str 7 ring B str 6 N-H ip B 15 C-H ip BC	1596 (5)	12 BC str 23 AB str 18 ring B str 7 C-H ip BC 6 C-H ip AB
1560 (22)	25 N-H ip B 24 N-H ip C	1572 (27)	23 N-H ip B 35 N-H ip C	1558 (26)	25 N-H ip B 21 N-H ip C 15 ring B 7 A-B
1529 (20)	6 N-H ip A 7 N-H ip B 17 N-H ip C 9 AB str 8 ring B str 7 CD str 5 ring C str 5 C-H ip AB	1536 (4)	52 ring B str 6 B bend	1545 (12)	31 ring B str 7 BC str 8 AB str 5 ring B bend 7 N-H ip C
1515 (6)	40 ring C str 7 ring B str	1530 (14)	9 N-H ip A 7 N-H ip B 18 N-H ip C 6 C-H ip AB 7 C- H ip BC 11 A-B str	1523 (12)	8 ring A str 7 AB str 6 ring C str 7 N-H ip A 12 N-H ip B 16 N-H ip C 5 C-H ip AB
1504 (7)	44 ring B str 8 ring C str	1500 (3)	39 ring C str	1501 (6)	46 ring C str

Frequencies (ν) are given in cm^{-1}; the relative intensities (I, in parentheses) refer to the strongest band (= 100). The normal mode compositions are given in terms of the PED (in %), restricted to coordinates with a PED > 5%. AB str, BC str, and CD str refer to the stretching coordinates of the A-B, B-C, and C-D methine bridges, respectively; C-H ip CD, C-H ip BC, C-H ip AB refer to C-H in-plane bending of the respective C-D, B-C, and A-B methine bridge hydrogens; ring A str, ring B str, ring C str, ring D str, refer to carbon-carbon stretchings of the respective pyrrole rings; ring A bend, ring B bend, ring C bend, ring D bend refer to bending the respective pyrrole rings; N-H ip A, N-H ip B, N-H ip C, N-H ip D refer to N-H in-plane bending of ring A, B, C, and D, respectively. *Data taken from Murgida et al. (21).

experimental RR spectrum. One of the few modes that in the M-HSE model shows a better agreement with the experimental spectrum refers to the N-H in-plane bending of rings B and C (1570 cm^{-1}; Fig. 5), although the corresponding mode of the M-HSD model still lies within the error margin for DFT calculations of organic molecules (32–34).

Isotopic shifts

The QM/MM calculations also reproduce the spectral changes induced by isotopic labeling of the chromophore. For the ^{13}C labeling at the C(5) position (A-B methine bridge), the main effects are observed in the marker band region (Fig. 6). In the experimental spectrum of Cph1Δ2 in solution, we note the disappearance of the shoulder at 1649 cm^{-1}, which confirms the assignment of this band to the A-B stretching mode. For the M-HSD model, this mode is calculated to shift down from 1644 to 1630 cm^{-1} such that it essentially coincides with the C-D methine bridge stretching at 1628 cm^{-1}. The latter mode remains unaffected upon ^{13}C labeling at the C(5) position. As a result, the calculated spectrum displays only a single peak. Also in the

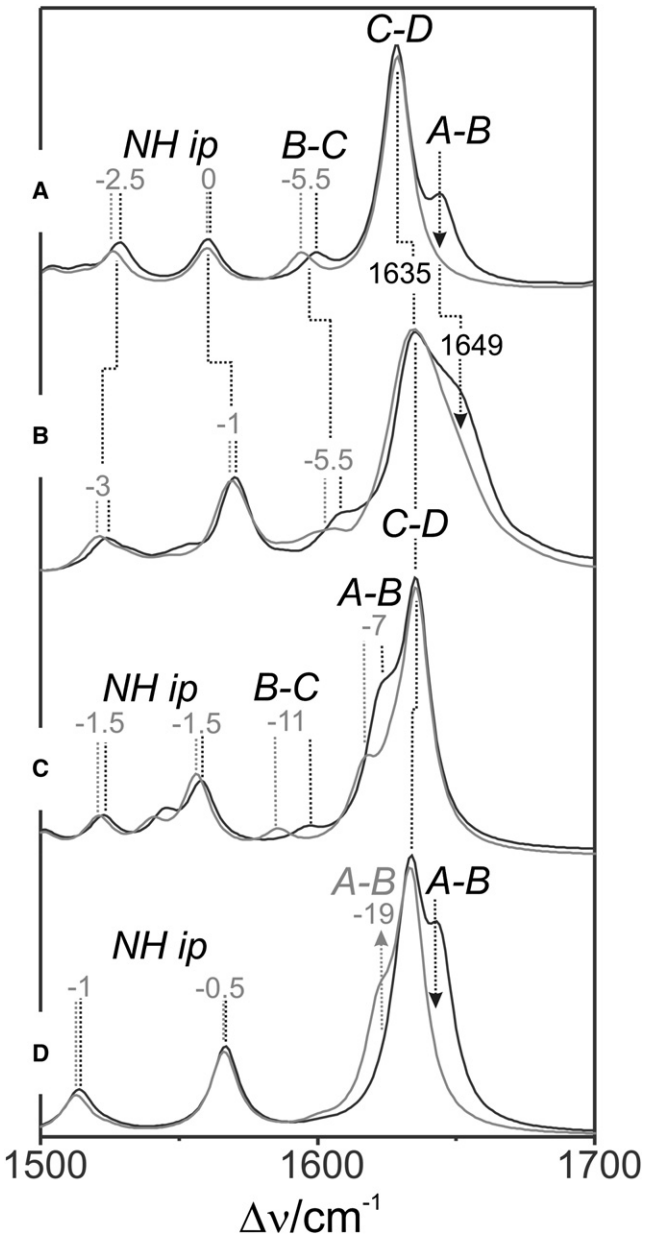

FIGURE 6 Experimental RR spectra of the Pr state of Cph1Δ2 compared with calculated Raman spectra. (*A*) Calculated Raman spectrum of M-HSD model obtained by QM/MM calculations. (*B*) Experimental RR spectrum of a frozen Cph1Δ2 solution. (*C*) Calculated Raman spectrum of the isolated PCB in the ZZZssa geometry obtained by QM calculations. (*D*) Calculated Raman spectrum of the isolated PCB in the ZZZasa geometry obtained by QM calculations. The black and gray traces refer to Cph1Δ2 adducts with nonlabeled PCB and PCB ^{13}C labeled at position C5, respectively. Gray numbers refer to isotopic shifts. The QM-calculated spectra were taken from Murgida et al. (21).

experimental spectrum, the position of the main peak at 1635 cm^{-1} remains unchanged; however, the band profile is clearly asymmetrical with residual intensity on the high-frequency side. It is possible that the actual downshift of the 1649-cm^{-1} band in the experimental RR spectrum is somewhat smaller than the calculated one, and thus may account for RR intensity at ~1640 cm^{-1}. Furthermore, the Pr chromophore in the frozen solution may be conformationally heterogeneous, as implied by the width of the peak at 1635 cm^{-1}, which is larger by a factor of 2 as compared with the corresponding band width in the crystalline state (Fig. 5). As a result, the bands originating from the A-B and C-D stretching modes may be broadened due to heterogeneity and thus can readily account for the unusual peak shapes and widths in the spectra of the samples with unlabeled and ^{13}C(5)-labeled cofactors. Note that these isotopic effects are quite similar to those observed for phyA-PCB adducts (21).

Furthermore, the predicted downshifts of the B-C stretching (−5.5 cm^{-1}) and the N-H in-plane (out-of-phase) bending (−2.5 cm^{-1}) agree very well with the experimental data. This is also true for the few notable isotopic shifts in the low-frequency region that refer to the weak bands at 762 cm^{-1} (−2 cm^{-1}) and 720 cm^{-1} (−4 cm^{-1}) and are readily compared with the calculated downshifts of the bands 755 and 727 cm^{-1} by −4 and −3 cm^{-1}, respectively (Fig. S11). Also, the ^{15}N/^{14}N- and H/D-induced shifts, mainly observed in the marker band region, are consistent with the calculations (Fig. S12).

QM versus QM/MM calculations

Although the QM/MM calculations (specifically of the M-HSD model) provide a very good description of the experimental RR spectra of the Pr state of Cph1Δ2, QM calculations of the isolated chromophore in vacuo yield contradictory results that led to erroneous conclusions in our previous studies (21) (Fig. 6). For the isolated PCB in the ZZZssa configuration, corresponding to the overall chromophore geometry in the crystal structure, the calculated Raman spectrum does not reproduce the characteristic two-banded pattern in the marker band region with the prominent C-D stretching flanked by a weaker band on the high-frequency side. Instead, these QM calculations predict the A-B stretching to be at a distinctly lower frequency than the C-D stretching, such that neither the experimental spectra nor the experimental isotopic shifts are reproduced. In this respect, a much better agreement is achieved on the basis of QM calculations for the isolated cofactor in the ZZZasa configuration for which the correct order of the C-D and A-B stretching is predicted, and in addition the isotopic shifts are well reproduced. Thus, the QM-calculated Raman spectrum of the isolated cofactor in the ZZZasa configuration coincidentally provides a mode pattern in the marker band region similar to the QM/MM-calculated spectrum of the ZZZssa chromophore in the protein (cf. Murgida et al. (21)).

Effect of protein-cofactor interactions on the RR spectrum of the chromophore

To analyze the effect of the protein environment on the RR spectrum of the cofactor, we first compare the chromophore

TABLE 2 Structural parameters of the methine bridges of the protein-bound PCB in the M-HSD and M-HSE models, and the isolated PCB in the ZZZssa and ZZZasa configuration

	QM/MM calculations		QM calculations*	
A-B methine bridge	M-HSD	M-HSE	ZZZssa	ZZZasa
Bond lengths (Å)				
C(A) = C	1.360	1.363	1.371	1.357
C-C(B)	1.428	1.428	1.429	1.443
Bond and dihedral angles (degree)				
C(A) = C-C(B)	129.32	129.95	135.26	129.17
N(A)C(A) = CC(B)	−5.01	2.34	−7.87	−2.93
C(A)C-C(B)N(B)	17.02	13.05	10.47	148.30
B-C methine bridge				
Bond lengths (Å)				
C(B)-C	1.394	1.391	1.393	1.394
C-C(B)	1.391	1.404	1.401	1.398
C-C(B)				
Bond and dihedral angles (degree)	134.09	136.02	136.47	134.03
N(B)C(B) = CC(C)	2.83	−0.41	1.74	1.50
C(B)C-C(C)N(C)	−6.172	2.76	6.88	1.26
C-D methine bridge				
Bond lengths (Å)				
C(C) = C	1.435	1.444	1.440	1.440
C-C(D)	1.363	1.366	1.362	1.362
Bond and dihedral angles (degree)				
C(C) = C-C(D)	126.59	130.64	131.14	130.68
N(C)C(C) = CC(D)	−150.56	−156.83	154.75	154.65
C(C)C-C(D)N(D)	8.87	4.27	−1.32	−2.2

Structural formulas for the ZZZssa and ZZZasa configurations are shown in Fig. 1 and Fig. S9.
*Taken from Murgida et al. (21)

structures optimized for the M-HSD model and the isolated PCB in the ZZZssa geometry obtained by QM/MM and QM calculations, respectively (Table 2). Here, we concentrate on the structural and electronic parameters of the methine bridges that are expected to be the main determinants for the vibrational spectrum in the marker band region. For the A-B methine bridge, we note a decrease of the C=C bond length from 1.371 Å in the isolated PCB to 1.360 Å in the M-HSD model, whereas the C-C bond length remains unchanged (1.429 vs. 1.428 Å). The B-C methine bridge reveals the opposite behavior inasmuch as the two bond lengths are nearly the same (1.394 and 1.391 Å) in the M-HSD model, in contrast to the isolated cofactor (1.393 vs. 1.401 Å). For the C-D methine bridge, the respective bond lengths are very similar for the isolated cofactor and the protein-bound PCB. These findings imply that within the M-HSD model the protein-cofactor interactions enhance and weaken the bond length alternation of the A-B and B-C methine bridge, respectively. As a consequence, the conjugation decreases at the A-B bridge but increases at the B-C bridge, as indeed reflected by the Wiberg indices (Table S2). Thus, the intrinsic A-B double-bond stretching frequency, i.e., the frequency of a pure A-B stretching mode, should be higher in the M-HSD model than in the isolated cofactor, whereas the opposite tendency is expected for the corresponding B-C stretching. Accordingly, the modes of predominantly A-B and B-C stretching character are widely separated in the M-HSD model and give rise to two bands at 1645 and 1599 cm^{-1} of medium and low Raman intensity, respectively (Table 1). For the isolated cofactor, however, the intrinsic A-B and B-C stretching frequencies approach each other such that the corresponding coordinates are distributed between two modes at 1622 and 1596 cm^{-1}.

Within this scheme, the spectra calculated for the M-HSE model and the isolated cofactor in the ZZZasa geometry can also be rationalized. For the M-HSE model, the bond length pattern of the B-C methine bridge is very similar to that of the isolated cofactor, whereas the A-B methine bridge changes are comparable to those of the M-HSD model, albeit less pronounced (Table 2). Again, this is also reflected in the Wiberg indices. Thus, mixing of the A-B and B-C stretching coordinates is weak, but the frequency of the largely pure A-B stretching is not as high (1635 cm^{-1}) as in the M-HSD model (Table 1). The isolated cofactor in the ZZZasa geometry displays a qualitatively similar picture with respect to methine bridge bond lengths and Wiberg indices, although the loss of conjugation in the A-B bridge is even more pronounced and the A-B stretching frequency is as high as in the M-HSD model.

One possible origin of the changes in the methine bridge conjugation may be steric interactions with the protein matrix, which may cause subtle distortions in the tetrapyrrole geometry. However, there is no correlation with deviations in the coplanarity between adjacent pyrrole rings and the methine bridge conjugations. Instead, the most striking geometric difference refers to the A-B methine bridge bond angle, which is distinctly wider for the isolated cofactor in the ZZZssa geometry (135.26°) as compared with that for the M-HSD and M-HSE models and the isolated PCB in the ZZZasa configuration, which all exhibit bond angles between 129 and 130°. A closer inspection of the data for the A-B methine bridge bond angle and the frequency of the A-B stretching mode reveals an inverse linear relationship that holds for PCB structures in both the ZZZssa and ZZZasa geometries (Fig. S10). Here, the QM-calculated structures represent the limiting cases, with the smallest bond angle and highest frequency for the (strained) ZZZasa, and the largest bond angle and lowest frequency for the ZZZssa geometry. Interestingly, the QM/MM calculations of the corresponding protein-PCB complexes of Cph1Δ2 (ZZZssa) and α-CPC (ZZZasa (36)) reveal opposite effects of the protein environment: the A-B methine bridge bond angle decreases in α-CPC (36) but increases in Cph1Δ2 as compared with the isolated cofactors. As a result, the A-B stretching frequency is lowered by ~20 cm^{-1} in α-CPC and raised by ~40 cm^{-1} in Cph1Δ2, providing a very good description of the respective experimental data.

In Cph1Δ2 the decrease of the A-B methine bridge bond angle is most likely related to the specific hydrogen bond network involving the N-H groups of rings A, B, and C (29). In the M-HSE and M-HSD models, the N-H group of ring B is hydrogen bonded to the carbonyl function of Asp^{207}, whereas the N-H group of ring A interacts with His^{260} via one water and two water molecules in the M-HSE and M-HSD model, respectively (Fig. 3). The ring C N-H group undergoes interactions similar to those of rings B and A in the M-HSE and M-HSD model, respectively. In contrast to these complex networks, the simplified QM model of PCB displays relatively symmetric interactions of the three N-H groups with the central counterion, which, after geometry optimization, is positioned nearly equidistant to the ring A, B, and C nitrogens.

The second major spectral difference in the marker band region refers to the C-D stretching mode that decreases in frequency in the order QM(ZZZssa) > M-HSD > M-HSE. In this case, correlations between structural parameters and mode frequencies are not obvious because the mode compositions are quite different for the M-HSE and M-HSD model. In the M-HSE and QM models, the C-D stretching coordinate is largely concentrated in one mode. The M-HSD model, however, displays two closely spaced modes, both of which are dominated by the C-D stretching and a C=C stretching of ring D.

In addition, the quite substantial frequency variations of the C-H out-of-plane deformation mode of the C-D methine bridge cannot readily be rationalized (Fig. 4). In particular, the tilt angle of ring D, which has been proposed to be a crucial parameter controlling the frequency and intensity of this mode (8,10), does not differ substantially between the various QM/MM and QM models.

On the other hand, most of the remaining spectral differences between the M-HSD and M-HSE models can in principle be understood inasmuch as they refer to regions that include modes involving the N-H out-of-plane deformation (670–700 cm^{-1}) as well as the C-N stretching and N-H in-plane bending coordinates (1200–1350 cm^{-1}; 1570 cm^{-1}). These are modes that should most sensitively reflect the differences in the hydrogen bond networks associated with the N-H groups of rings A, B, and C (vide supra).

Structure refinement on the basis of RR spectroscopy and QM/MM calculations

Both the M-HSD and M-HSE models are based on the same amino acid skeleton provided by the crystal structure analysis of Cph1Δ2 (29). Initial structures for the MD simulations differ only by the protonation site of His^{260}, and optimization leads to differences mainly in the hydrogen bond network in the chromophore-binding pocket, associated with minor structural changes of the cofactor and subtle displacements of nearby amino acids. The crystal structure does not provide direct information for the correct placement of protons. Furthermore, the amino acid framework that is finally obtained in the QM/MM-optimized structures for both models is compatible with the x-ray diffraction data, taking into account the experimental resolution of 2.45 Å. On the other hand, the Raman spectrum of the M-HSD model provides a better reproduction of the experimental RR spectra of Cph1Δ2 than the M-HSE model. This is true for Cph1Δ2 in both solution and the crystalline state. Thus, we conclude that M-HSD represents an improved structural model for the chromophore-binding pocket in the Pr state of Cph1Δ2 that specifically provides a more substantiated description of the internal hydrogen-bond network. Taking into account that our analysis is based on the initial modification of only one structural parameter, i.e., the protonation site of His^{260} and thus effectively the rotation its imidazole ring by 180°, one may well imagine that further improvements can be achieved by future systematic variations of other structural parameters.

CONCLUSIONS

The QM/MM methodology allows for a good description of the experimental RR spectra of the Pr state of Cph1Δ2. The calculated spectra reflect the distortions of the chromophore geometry induced by the interactions with the protein environment. The distortions primarily include a narrowing of the bond angle of the A-B methine bridge as compared with the geometry of the isolated PCB obtained by QM calculations. As a result, the corresponding A-B stretching mode is predicted to be higher by ~40 cm^{-1} in the QM/MM than in the QM calculations. It is shown that the A-B stretching frequency displays an inverse linear relationship with the A-B bond angle.

Because of this protein-induced distortion at the A-B methine bridge, QM calculations of isolated PCB in the ZZZssa geometry fail to reproduce the experimental RR spectra of the Pr chromophore, which is the main origin of the erroneous assignment of the cofactor structure in our previous study on phyA (21).

The experimental RR spectra of Cph1Δ2 in the crystalline state and in frozen solutions indicate the same overall chromophore geometry. However, there are subtle conformational differences and a higher conformational heterogeneity of the chromophore in solution.

Compared with the M-HSE model, a better reproduction of the experimental RR spectra of the Pr state of Cph1Δ2 is achieved on the basis of the M-HSD model, indicating that it represents an improved structural model for the chromophore-binding pocket. A more systematic study that, in addition to the protonation site of His^{260}, includes further structural degrees of freedom in the chromophore-binding pocket may therefore lead to a refinement of the crystal structure model in the chromophore cavity, including the hydrogen-bond network.

In that respect, this work introduces a combined theoretical (QM/MM) and experimental (RR) concept to

complement and refine crystallographic structural models of cofactor-protein complexes in general.

SUPPORTING MATERIAL

Twelve figures and two tables are available at http://www.biophysj.org/biophysj/supplemental/S0006-3495(09)00587-6.

We thank the Norddeutscher Verbund für Hoch und Höchstleistungsrechnen and Prof. Walter Thiel from the Max Planck Institut für Kohlenforschung (Mülheim an der Ruhr) for providing computational resources. Financial support by the Deutsche Forschungsgemeinschaft (SFB 498; Excellence Cluster ''Unifying Concepts in Catalysis''; Hu702/6, Es152/6) is gratefully acknowledged.

REFERENCES

1. Briggs W. R. and Spudich J. L. editors. (2005). Handbook of Photosensory Receptors. Wiley-VCH, Weinheim, Germany.
2. Hughes, J., T. Lamparter, F. Mittmann, E. Hartmann, W. Gärtner, et al. 1997. A prokaryotic phytochrome. *Nature*. 386:663.
3. Rockwell, N. C., Y. S. Su, and J. C. Lagarias. 2006. Phytochrome structure and signalling mechanisms. *Annu. Rev. Plant Biol.* 57:837–858.
4. Rüdiger, W., F. Thümmler, E. Cmiel, and S. Schneider. 1983. Chromophore structure of the physiological active form Pfr of phytochrome. *Proc. Natl. Acad. Sci. USA*. 80:6244–6248.
5. Fodor, S. P. A., J. C. Lagarias, and R. A. Mathies. 1988. Resonance Raman-spectra of the Pr-form of phytochrome. *Photochem. Photobiol.* 48:129–136.
6. Tokutomi, S., Y. Mizutani, H. Anni, and T. Kitagawa. 1990. Resonance Raman-spectra of large pea phytochrome at ambient-temperature—difference in chromophore protonation between red-absorbing and far red-absorbing forms. *FEBS Lett.* 269:341–344.
7. Hildebrandt, P., A. Hoffmann, P. Lindemann, G. Heibel, S. E. Braslavsky, et al. 1992. Fourier-transform resonance Raman spectroscopy of phytochrome. *Biochemistry*. 31:7957–7962.
8. Fodor, S. P. A., J. C. Lagarias, and R. A. Mathies. 1990. Resonance Raman analysis of the Pr and Pfr forms of phytochrome. *Biochemistry*. 29:11141–11146.
9. Mizutani, Y., S. Tokutomi, K. Aoyagi, K. Horitsu, and T. Kitagawa. 1991. Resonance Raman-study on intact pea phytochrome and its model compounds—evidence for proton migration during the phototransformation. *Biochemistry*. 30:10693–10700.
10. Matysik, J., P. Hildebrandt, W. Schlamann, S. E. Braslavsky, and K. Schaffner. 1995. Fourier-transform resonance Raman spectroscopic study of the intermediate states of phytochrome. *Biochemistry*. 34:10497–10507.
11. Andel III, F., J. C. Lagarias, and R. A. Mathies. 1996. Resonance Raman analysis of chromophore structure in the lumi-R photoproduct of phytochrome. *Biochemistry*. 35:15997–16008.
12. Kneip, C., D. Mozley, P. Hildebrandt, W. Gärtner, S. E. Braslavsky, et al. 1997. Effect of chromophore exchange on the resonance Raman spectra of recombinant phytochromes. *FEBS Lett.* 414:23–26.
13. Remberg, A., I. Lindner, T. Lamparter, J. Hughes, C. Kneip, et al. 1997. Spectral and light-induced kinetic characterization of a recombinant phytochrome of the cyanobacterium. *Synechocystis*. *Biochemistry*. 36:13389–13395.
14. Kneip, C., P. Hildebrandt, W. Schlamann, S. E. Braslavsky, F. Mark, et al. 1999. Protonation state and structural changes of the tetrapyrrole chromophore during the $P_r \rightarrow P_{fr}$ phototransformation of phytochrome. A resonance Raman spectroscopic study. *Biochemistry*. 38:15185–15192.
15. Hildebrandt, P., C. Kneip, J. Matysik, K. Nemeth, I. Magdo, et al. 1999. Vibrational analysis of linear tetrapyrroles. Implications for interpreting the resonance Raman spectra of phytochrome. *Rec. Res. Dev. Phys. Chem.* 3:63–77.
16. Kneip, C., K. Nemeth, F. Mark, P. Hildebrandt, and K. Schaffner. 1999. Interpretation of the resonance Raman spectra of linear tetrapyrroles based on DFT calculations. Implications for the structure and protonation state of the chromophore in phytochrome. *Chem. Phys. Lett.* 311:479–484.
17. Kneip, C., W. Schlamann, S. E. Braslavsky, and P. Hildebrandt. 2000. Resonance Raman spectroscopic study of the tryptic 39kDa fragment of phytochrome. *FEBS Lett.* 482:252–256.
18. Mroginski, M. A., D. H. Murgida, D. von Stetten, C. Kneip, F. Mark, et al. 2004. Determination of the chromophore structures in the photoinduced reaction cycle of phytochrome. *J. Am. Chem. Soc.* 126:16734–16735.
19. Borucki, B., D. von Stetten, S. Seibeck, T. Lamparter, N. Michael, et al. 2005. Light-induced proton release of phytochrome is coupled to the transient deprotonation of the tetrapyrrole chromophore. *J. Biol. Chem.* 280:34358–34364.
20. Mroginski, M. A., D. H. Murgida, and P. Hildebrandt. 2007. The chromophore structural changes during the photocycle of phytochrome: a combined resonance Raman and quantum chemical approach. *Acc. Chem. Res.* 40:258–266.
21. Murgida, D. H., D. von Stetten, P. Hildebrandt, P. Schwinté, F. Siebert, et al. 2007. The chromophore structures of the Pr states in plant and bacterial phytochromes. *Biophys. J.* 93:2410–2417.
22. von Stetten, D., S. Seibeck, N. Michael, P. Scheerer, M. A. Mroginski, et al. 2007. Highly conserved residues D197 and H250 in Agp1 phytochrome control the proton affinity of the chromophore and Pfr formation. *J. Biol. Chem.* 282:2116–2123.
23. Ulijasz, A. T., G. Cornilescu, D. von Stetten, S. Kaminski, M. A. Mroginski, et al. 2008. Characterisation of two thermostable cyanobacterial phytochromes reveal global movements in the chromophore-binding domain during photconversion. *J. Biol. Chem.* 283:21251–21266.
24. von Stetten, D., M. Günther, P. Scheerer, D. H. Murgida, M. A. Mroginski, et al. 2008. Chromophore heterogeneity and photoconversion in phytochrome crystals and solutions studied by resonance Raman spectroscopy. *Angew. Chem. Int. Ed.* 47:4753–4755.
25. Wagner, J. R., J. Zhang, D. von Stetten, M. Günther, D. H. Murgida, et al. 2008. Mutational analysis of *Deinococcus radiodurans* bacteriophytochrome reveals key amino acids necessary for structural integrity and the proton exchange cycle during photoconversion. *J. Biol. Chem.* 283:12212–12226.
26. Wagner, J. R., J. S. Brunzelle, K. T. Forest, and R. D. Vierstra. 2005. A light-sensing knot revealed by the structure of the chromophore-binding domain of phytochrome. *Nature*. 438:325–331.
27. Wagner, J. R., J. R. Zhang, J. S. Brunzelle, R. D. Vierstra, and K. T. Forest. 2007. High resolution structure of Deinococcus bacteriophytochrome yields new insights into phytochrome architecture and evolution. *J. Biol. Chem.* 282:12298–12309.
28. Yang, X., E. A. Stojkovic, J. Kuk, and K. Moffatt. 2007. Crystal structure of the chromophore binding domain of an unusual bacteriophytochrome, RpBphP3, reveals residues that modulate photoconversion. *Proc. Natl. Acad. Sci. USA*. 104:12571–12576.
29. Essen, L. O., J. Hughes, and J. Mailliet. 2008. The structure of a complete phytochrome sensory module in the Pr ground state. *Proc. Natl. Acad. Sci. USA*. 105:14709–14714.
30. van Thor, J. J., M. Mackeen, I. Kuprow, R. A. Dwek, and M. R. Wormold. 2006. Chromophore structure in the photocycle of the cyanobacterial phytochrome Cph1. *Biophys. J.* 91:1811–1822.
31. Hahn, J., H. M. Strauss, and P. Schmieder. 2008. Heteronuclear NMR investigation on the structure and dynamics of the chromophore binding pocket of the cyanobacterial phytochrome Cph1. *J. Am. Chem. Soc.* 130:11170–11178.
32. Magdo, I., K. Nemeth, F. Mark, P. Hildebrandt, and K. Schaffner. 1999. Calculation of vibrational spectra of linear tetrapyrroles. 1. Global sets of scaling factors for force fields derived by ab initio and density functional theory. *J. Phys. Chem. A*. 103:289–303.

33. Mroginski, M. A., K. Nemeth, T. Bauschlicher, W. Klotzbucher, R. Goddard, et al. 2005. Calculation of vibrational spectra of linear tetrapyrroles. 3. Hydrogen-bonded hexamethylpyrromethene dimers. *J. Phys. Chem. A.* 109:2139–2150.

34. Mroginski, M. A., D. H. Murgida, and P. Hildebrandt. 2006. Calculation of vibrational spectra of linear tetrapyrrols. 4. Methine bridge C-H out-of-plane modes. *J. Phys. Chem. A.* 110:10564–10574.

35. Shurki, A., and A. Warshel. 2003. Structure / function correlations of proteins using MM, QM/MM, and related approaches: methods, concepts, pitfalls, and current progress. *Adv. Protein Chem.* 66:249–313.

36. Mroginski, M. A., F. Mark, W. Thiel, and P. Hildebrandt. 2007. Quantum mechanics / molecular mechanics calculation of the Raman spectra of the phycocyanobilin chromophore in α-C-phycocyanin. *Biophys. J.* 93:1885–1894.

37. Landgraf, F. T., C. Forreiter, A. Hurtado Pico, T. Lamparter, and J. Hughes. 2001. Recombinant holophytochrome in *Escherichia coli*. *FEBS Lett.* 508:459–462.

38. Makhynya, Y., Z. Hussain, T. Bauschlicher, P. Schwinté, F. Siebert, et al. 2007. Synthesis of selectively ^{13}C-labelled bilin compounds. *Eur. J. Org. Chem.* 8:1287–1293.

39. Strauss, H. M., J. Hughes, and P. Schmieder. 2005. Heteronuclear solution state NMR studies of the chromophore in cyanobacterial phytochrome Cph1. *Biochemistry.* 44:8244–8250.